## SUPPLEMENTARY FIGURE LEGENDS

**Supplementary figure 1. Cell cycle analysis of asynchronous *Lmna*$^{+/+}$ and *Lmna*$^{-/-}$ MEFs.** Asynchronously growing cells were harvested and fixed in 70% ethanol, followed by treatment with propidium iodide and 100 U/ml of RNase A. At least 10,000 cells were scored using a FACScan flow cytometer. Cell cycle distribution was analyzed with Cell Quest software. No differences in cell cycle distribution were observed upon loss of A-type lamins.

**Supplementary figure 2. Telomerase activity and binding of TRF1, TRF2 and A-type lamins to telomeres in wild-type and *Lmna*$^{-/-}$ MEFs.** (**A**) Telomerase activity in cellular extracts was compared between wild-type and *Lmna*$^{-/-}$ MEFs (see methods), with no significant changes observed between the two genotypes. The graph shows the quantitation of four independent experiments. Bars represent standard error. (**B**) Chromatin immunoprecipitation (ChIP) analysis to monitor the binding of the shelterin complex components TRF1 and TRF2, and A-type lamins to telomeres in *Lmna*$^{+/+}$ and *Lmna*$^{-/-}$ MEFs. The top panel shows one representative experiment. The graph shows the quantification of immunoprecipitated telomeric repeats after normalization to input signals in two independent experiments. Note that the telomere-bound levels of TRF1 and TRF2 are indistinguishable between *Lmna*$^{-/-}$ and wild-type controls. In addition, A-type lamins are enriched at telomeres in wild-type MEFs. The bottom panel shows immunoprecipitated DNA hybridized with a pericentric probe. The absence of major satellite repeat sequences upon immunoprecipitation with TRF1 and TRF2 antibodies shows the specificity of the ChIP assay. As expected, A-type lamins also associated with pericentric heterochromatin.

**Supplementary figure 3. Status of Rb family members in *Lmna*$^{-/-}$ MEFs.** (**A**) Immunoblotting showing the expression of lamin A and lamin C in wild-type and Rb triple knock-out (TKO) cells, but not in *Lmna*$^{-/-}$ MEFs (top). Immunoblotting with actin antibody shows equivalent amount of cell lysates used for the Rb family immunoprecipitation studies. (**B**) Immunoprecipitation of Rb family members with agarose-conjugated specific antibodies followed by immunoblotting to determine the levels of the different proteins in wild-type and *Lmna*$^{-/-}$ MEFs. Triple-knock out MEFs for Rb family members (TKO) were used as a negative control. Note the decrease in Rbl1 (p107) and Rbl2 (p130) levels in *Lmna*$^{-/-}$ MEFs. Rb1 levels were also undetected in *Lmna*$^{-/-}$ cells.

**Supplementary Figure 4. Alterations in the levels of TERRAs per telomeric repeats upon loss of A-type lamins and/or Rb family members.** (**A**) Total RNA from *Rb*$^{-/-}$, DKO and TKO MEFs was subjected to Northern blotting with a telomeric probe to monitor changes in the levels of TERRAs. Hybridization with a probe specific for 28S RNA shows equivalent levels of RNA isolated from both cell lines (bottom panels). MEFs derived from 2 embryos of each genotype were included in the analysis (A and B). The graph shows the quantification of the levels of TERRAs after normalization to levels of 28S in three independent experiments. Note the increasing levels of TERRAs levels upon loss of one, two or three Rb family members. (**B**) Representative TRF analysis of immortalized MEF lines devoid of Rb family members. Note the dramatic increment in telomere length upon loss of one, two or three Rb family members. (**C**) DNA dot blots of *Lmna*$^{+/+}$, *Lmna*$^{-/-}$, *Rb*$^{-/-}$, DKO and TKO MEFs hybridized with a telomeric (top) or a centromeric (bottom) probe. The graph shows the quantitation of three independent experiments after normalization of telomeric to centromeric signals. Note the increase in telomeric DNA content in Rb-deficient MEFs. Bars represent standard error. *represents p value of statistical significance. R.U. stands for relative units

**Supplementary figure 5. Genomic instability in *Lmna*$^{-/-}$ MEFs.**

(**A**) Quantification of signal free ends in metaphases from four different lines of *Lmna*$^{+/+}$ (1-4) and five different lines of *Lmna*$^{-/-}$ (A-E) MEFs. Note the increase in signal free ends in all the lines of *Lmna*$^{-/-}$ MEFs when compared to the different lines of wild-type MEFs. Images represent examples of chromosomes with signal free ends (arrows). (**B**) Quantification of the number of metaphases with chromosome and/or chromatid breaks in *Lmna*$^{+/+}$ (1-4) and *Lmna*$^{-/-}$ (A-E) lines. Images represent examples of breaks. A two-fold increase in breaks was observed in *Lmna*$^{-/-}$ lines. (**C**) Quantification of the number of end-to-end fusions in the nine different lines. Note the low number of fusions in both wild-type and *Lmna*$^{-/-}$ MEFs. Values are expressed as average ± standard error. *represents p value of statistical significance.

**Supplementary figure 6. Frequency of telomere recombination upon depletion of A-type lamins by CO-FISH. (A)** Table shows the frequencies of telomeric sister chromatid exchange events in *Lmna*$^{+/+}$ and *Lmna*$^{-/-}$ immortalized MEFs. Both, the frequencies of T-SCE events involving lagging (red) and leading (green) strands are shown. Note that loss of A-type lamins does not lead to changes in the frequency of recombination events involving telomeres. (**B**) Representative image of a metaphase labeled with leading and lagging strand probes. The enlarged image shows a sister chromatid exchange within telomeric DNA (T-SCE).

**Supplementary figure 7. Induction of DNA damage –telomere uncapping- upon expression of TRF2$^{\Delta B\Delta M}$. (A)** *Lmna*$^{+/+}$ and *Lmna*$^{-/-}$ MEFs retrovirally transduced with TRF2$^{\Delta B\Delta M}$ or GFP as control were processed for immunofluorescence with an antibody recognizing γH2AX (a marker of DNA damage). The percentage of cells presenting more than 5 foci of DNA damage was quantitated. Note that expression of TRF2$^{\Delta B\Delta M}$ leads to similar levels of DNA damage or telomere uncapping in both genotypes. **(B)** Western blots confirm the activation of the DNA damage response upon expression of TRF2$^{\Delta B\Delta M}$, as assessed by an increase in the levels of γH2AX with respect to GFP control.

Gonzalez-Suarez et al. Suppl Fig. 1

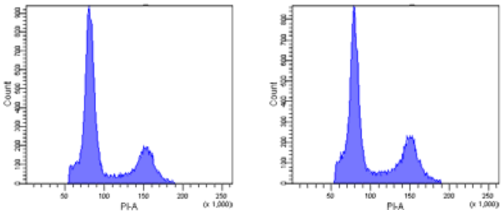

***Lmna*$^{+/+}$**

**GO/G1: 48.07%**

**G2/M: 20.95%**

**S: 30.98%**

***Lmna*$^{-/-}$**

**GO/G1: 57.73%**

**G2/M: 18.01%**

**S: 24.26%**

A

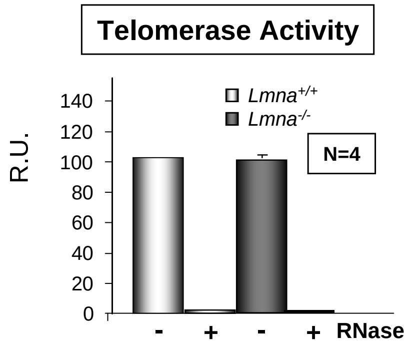
Telomerase Activity
R.U.
140
120
100
80
60
40
20
0
□ Lmna+/+
■ Lmna-/-
N=4
-
+
-
+
RNase

B

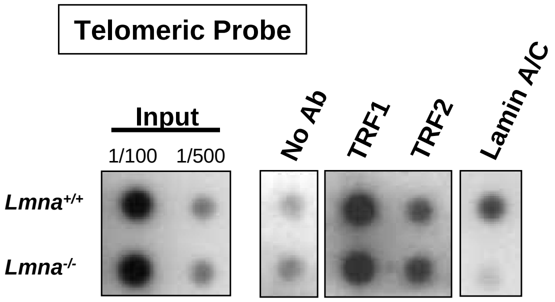
Telomeric Probe
Input
1/100
1/500
No Ab
TRF1
TRF2
Lamin A/C
Lmna+/+
Lmna-/-

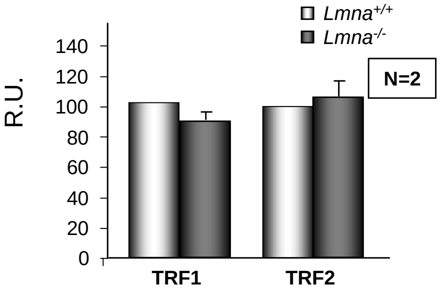
□ Lmna+/+
■ Lmna-/-
N=2
R.U.
140
120
100
80
60
40
20
0
TRF1
TRF2

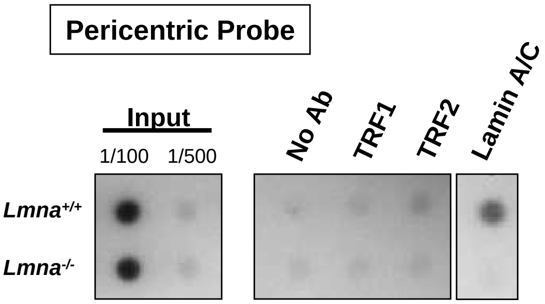
Pericentric Probe
Input
1/100
1/500
No Ab
TRF1
TRF2
Lamin A/C
Lmna+/+
Lmna-/-

Gonzalez-Suarez et al. Suppl Fig. 3

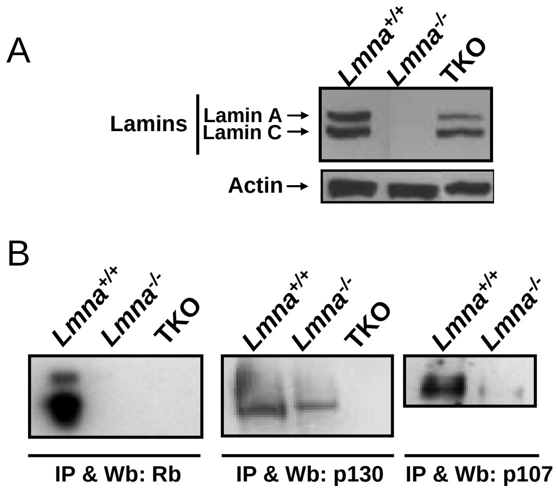

Gonzalez-Suarez et al. Suppl Fig. 4

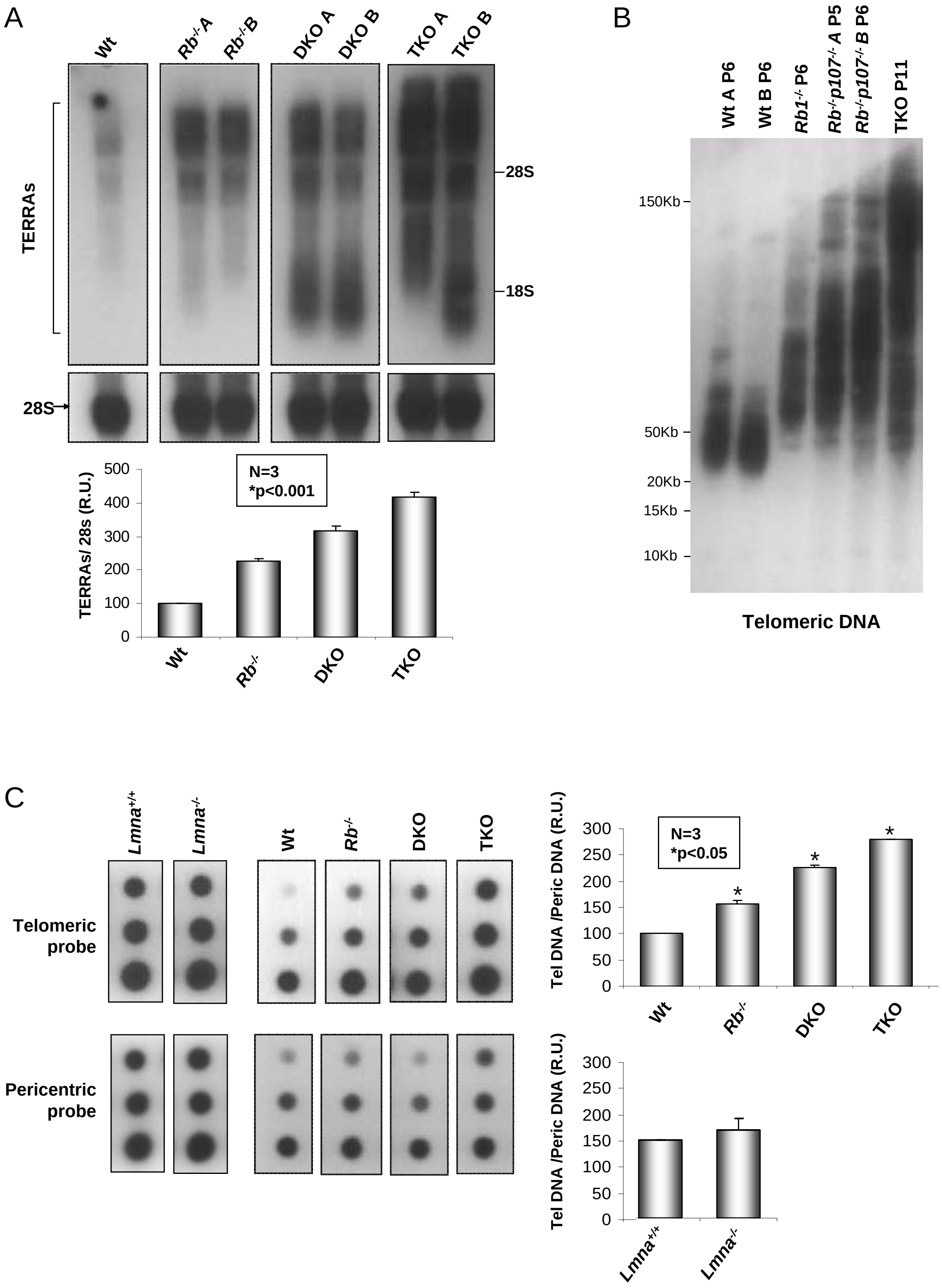

Gonzalez-Suarez et al. Suppl Fig. 5A

A

| ***Lmna***$^{+/+}$ | **Number of Metaphases** | **Total SFE** | **% Metaphases with SFE** | **Frequency SFE/chromosome** |
|---|---|---|---|---|
| **1** | 59 | 10 | 11.9 | 0.005±0.003 |
| **2** | 59 | 10 | 13.6 | 0.004±0.002 |
| **3** | 60 | 7 | 8.3 | 0.003±0.001 |
| **4** | 58 | 21 | 19.0 | 0.012±0.004 |
| **Total** | **236** | **48** | **13.2 ± 2.2** | **0.006 ± 0.001** |

| ***Lmna***$^{-/-}$ | **Number of Metaphases** | **Total SFE** | **% Metaphases with SFE** | **Frequency SFE/chromosome** |
|---|---|---|---|---|
| **A** | 60 | 39 | 36.7 | 0.009±0.003 |
| **B** | 52 | 33 | 40.7 | 0.011±0.003 |
| **C** | 55 | 22 | 29.1 | 0.017±0.004 |
| **D** | 56 | 52 | 51.8 | 0.018±0.003 |
| **E** | 58 | 28 | 32.8 | 0.024±0.004 |
| **Total** | **283** | **174** | **38.2 ± 3.9*** | **0.017 ± 0.002** |

**$^*p<0.001$**

**Normal Chromosomes**

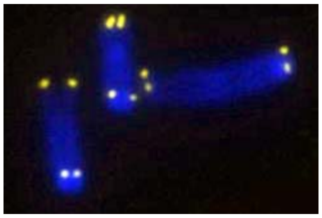

**Signal Free Ends**

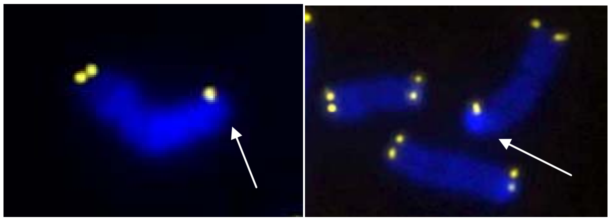

B

| *Lmna*$^{+/+}$ | Number of Metaphases | Total Breaks | % Metaphases with Breaks | Frequency Break/chromosome |
|---|---|---|---|---|
| **1** | 59 | 12 | 16.9 | 0.006±0.002 |
| **2** | 58 | 17 | 22.4 | 0.001±0.001 |
| **3** | 60 | 12 | 15.0 | 0.008±0.002 |
| **4** | 58 | 2 | 3.4 | 0.005±0.002 |
| **Total** | **236** | **43** | **14.4 ± 4.0** | **0.005 ± 0.001** |

| *Lmna*$^{-/-}$ | Number of Metaphases | Total Breaks | % Metaphases with Breaks | Frequency Break/chromosome |
|---|---|---|---|---|
| **A** | 60 | 22 | 23.3 | 0.015±0.003 |
| **B** | 52 | 25 | 38.5 | 0.011±0.003 |
| **C** | 55 | 22 | 20.0 | 0.012±0.003 |
| **D** | 56 | 12 | 16.1 | 0.005±0.003 |
| **E** | 58 | 30 | 51.7 | 0.006±0.002 |
| **Total** | **283** | **111** | **27.9 ± 4.0*** | **0.011 ± 0.001** |

***p<0.05**

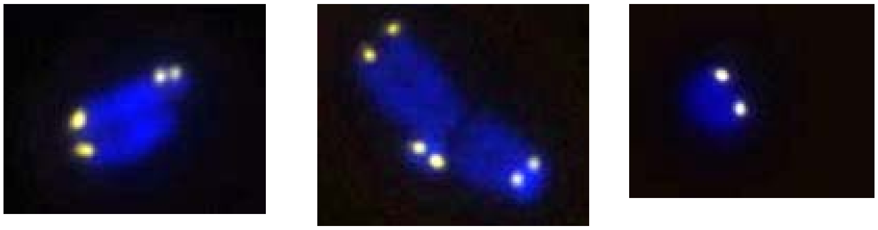

**Chromosome / Chromatid Breaks**

C

| *Lmna*$^{+/+}$ | Number of Metaphases | Total Fusions | % Metaphases with Fusions |
|---|---|---|---|
| **1** | 59 | 0 | 0.0 |
| **2** | 58 | 0 | 0.0 |
| **3** | 60 | 2 | 3.3 |
| **4** | 58 | 0 | 0.0 |
| **Total** | **236** | **2** | **0.8 ±1.6** |

| *Lmna*$^{-/-}$ | Number of Metaphases | Total Fusions | % Metaphases with Fusions |
|---|---|---|---|
| **A** | 60 | 0 | 0.0 |
| **B** | 52 | 3 | 5.7 |
| **C** | 55 | 0 | 0.0 |
| **D** | 56 | 0 | 0.0 |
| **E** | 58 | 1 | 1.7 |
| **Total** | **283** | **4** | **1.5 ± 1.0** |

A

| | Metaphases | Chromosomes | T-SCE (lagging) | Frequency T-SCE (lagging) | T-SCE (leading) | Frequency T-SCE (leading) | Frequency T-SCE |
|---|---|---|---|---|---|---|---|
| ***Lmna***$^{+/+}$ | 50 | 3398 | 126 | 0.037 | 136 | 0.040 | 0.077 |
| ***Lmna***$^{-/-}$ | 49 | 3465 | 99 | 0.029 | 127 | 0.037 | 0.066 |

B

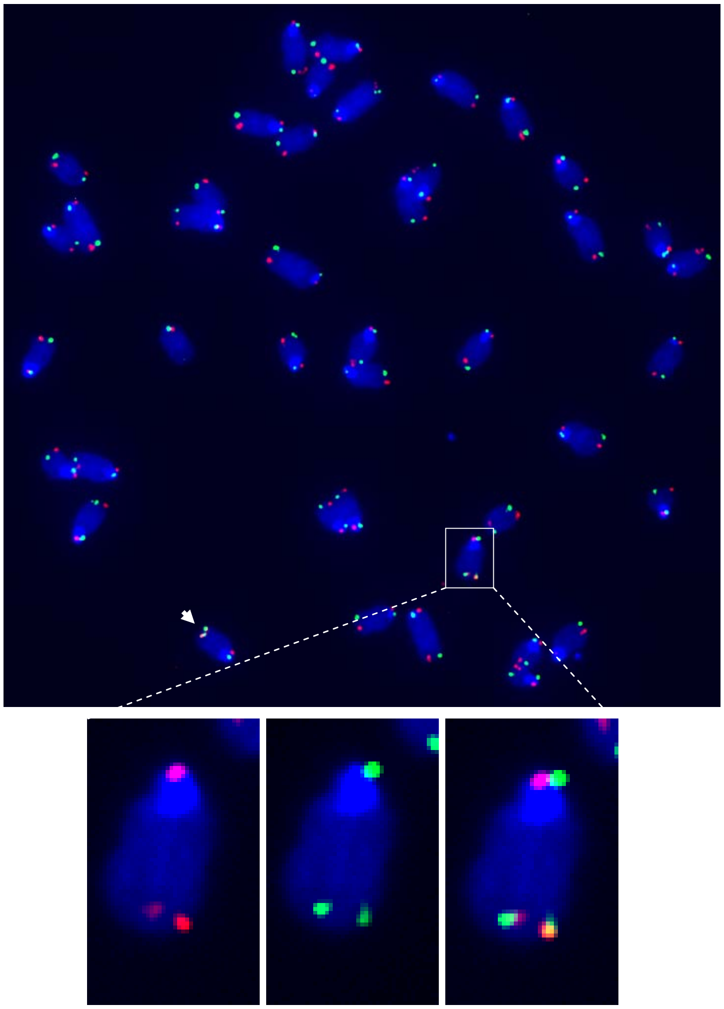

Gonzalez-Suarez et al. Suppl Fig. 7

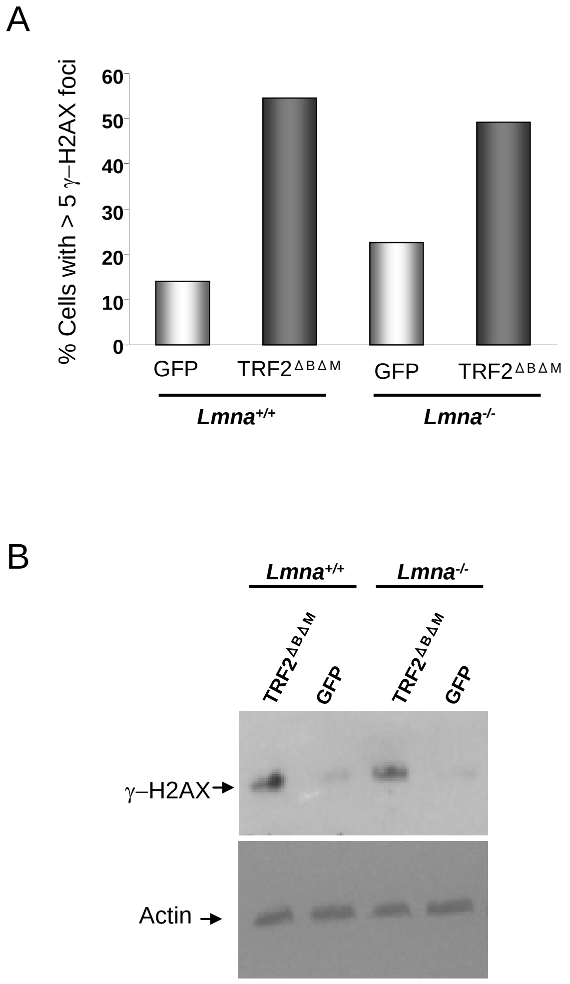

# SUPPLEMENTARY METHODS

## Distribution of the telomeres

To analyze the distribution of the telomeres we have chosen as metric; the shortest distance from the telomere to the edge of the convex hull [1], see figure 1. The fluorescent images of the telomere channel have been deconvolved, using in-house deconvolution software written in MatLab (The Mathworks, Natick, MA, USA). The MAPPG algorithm is chosen for devolving as described in [2]. The point spread function (PSF) used is an analytical PSF implemented according to [3]. After deconvolution, four steps are taken: 1. localization of the telomere signals, 2. computation of the convex hull, 3. computation of the distance transform within the convex hull, 4. extraction of the distance and intensity of the telomere fluorescent signal. All analyses have been done in 3D, but for clarification we have shown an example of the algorithms in 2D in figure 1. To determine the position of the telomeres we have used TeloView [4]. This program is especially designed to locate telomere FISH signals in images of fluorescently labeled nuclei. It uses a set of image processing algorithms from DIPimage, developed at the Quantitative Imaging Group (TU-Delft, The Netherlands, http://www.diplib.org) [5]. Both TeloView and DIPimage are implemented in MatLab. localization of the telomere signal, is performed as described in [6]. In short: after a scale space method, which enhances the contrast of the signal, a threshold is chosen to segment the telomere signals. Using the graphical interface of TeloView missed signals can be added or false signals can be removed. The second step is the calculation of the convex hull [1], which is the smallest convex volume enclosing all the found telomeres. For the next step we transform the hull into a distance matrix using the  Euclidian Distance Transform (EDT) [7, 8]. The EDT transforms the binary image (the convex hull image) into an image where the intensity level of the pixel is the shortest distance from this pixel to the edge of the hull.

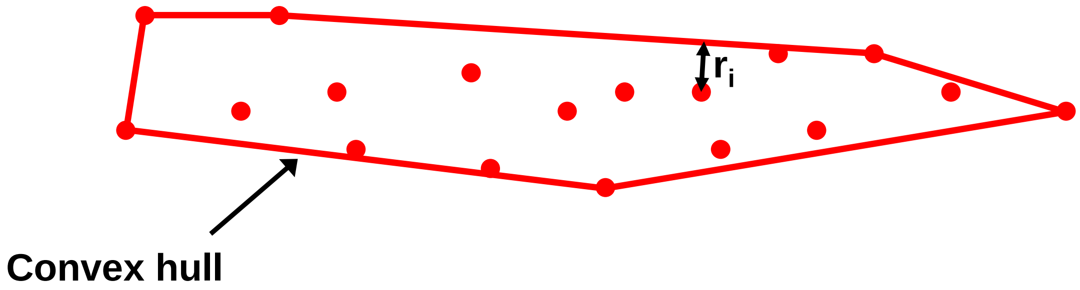

**Figure 1:** Cartoon showing the distance measure. The red dots represent the telomere signals. The red line represents the convex hull surrounding the telomeres. For every telomere we measure, $r_i$; the shortest distance from the surface of the convex hull to the telomere.

## Distribution of the telomere intensity

The fourth step is to calculate the integrated intensity of the telomere. The integrated intensity is proportional to the size of the telomere because the size is proportional to the amount of fluorochrome that is attached to the telomere and therefore to the telomere length [9]. We create a binary mask with the watershed algorithm [10] of the image data, *g*, convolved with a Gaussian profile with $\sigma = 1$ pixel for noise reduction. Now the telomere coordinates ($x_n$, $y_n$, $z_n$), determined above, tell us which objects in this mask are telomere regions. Simply integrating intensities in these regions will also give the wrong answer because background pixels are not excluded from these regions and will bias our calculations. Our solution is to calculate the integrated intensity in a region of interest with ($x_n$, $y_n$, $z_n$) as middle point within this mask resulting from the watershed. The region of interest is a small sphere, with radius *r*, convolved with a Gaussian profile with width $\sigma = 1$ pixel in the lateral and $\sigma = 3$ pixels in the axial direction, which results in an elongated sphere. We will call this region of interest, which is gray-scale, $sphere_{gray}$ and the region from the watershed, which is binary, we will call *mask*. The next binary region with which we work with is $sphere_{bin}$. This is a binary sphere with radius $r + 3\sigma$ (with $\sigma = 1$ or 3 pixels depending on the direction). Now we define the mean of the grey values of *g* at the coordinates where *mask* has value one and $sphere_{bin}$ has value zero as our background level, *b*. Our signal image, $g_{signal}$, becomes:

$$g_{signal} = g(mask) - b \tag{1}$$

We normalize both $sphere_{gray}$ and $g_{signal}$ for their maximum value and calculate their mean squared difference, $\varepsilon_{new}$, using $sphere_{gray}$ as a weighting function:

$$\varepsilon_{new} = \frac{\sum_i sphere_{gray,i}(sphere_{gray,i} - g_{signal})^2}{\sum_i sphere_{gray,i}} \tag{2}$$

This process starts with $r = 1$. First we rename $\varepsilon_{new}$:

$$\varepsilon_{old} = \varepsilon_{new} \tag{3}$$

Now we grow the region by using $r = r + 1$ for the next iteration and calculate $\varepsilon_{new}$ again. The iterative process is stopped when

$$\varepsilon_{new} > \varepsilon_{old} \tag{4}$$

The integrated intensity, $I_n$, for the $n^{th}$ telomere is now

$$I_n = \sum g_{signal}(sphere_{bin}) \tag{5}$$

In figure 2 we show a flow chart of the algorithm.

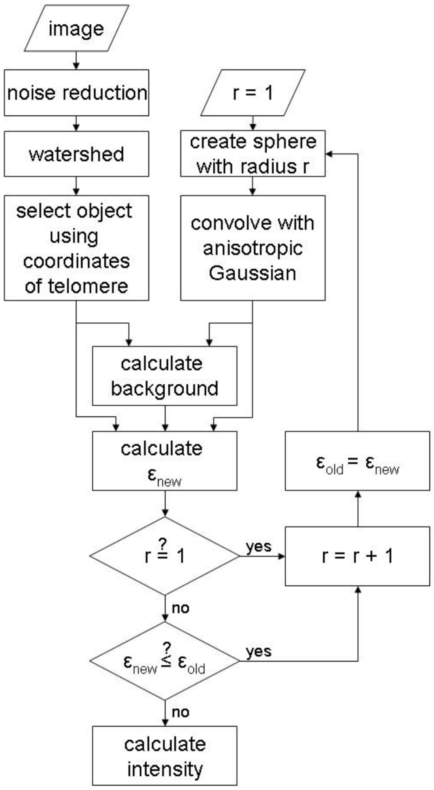

**Figure 2:** Flow chart showing the algorithm to calculate the integrated intensity of a telomere signal. The basic idea is to calculate the integrated intensity in a growing region of interest until no more intensity is added. The growing is confined by a mask created by a watershed.

## References

1. Barber, C.B., D.P. Dobkin, and H. Huhdanpaa, *The Quickhull algorithm for convex hulls.* ACM Transactions on Mathematical Software, 1996. **22**(4): p. 469-483.
2. Verveer, P.J. and T.M. Jovin, *Efficient superresolution restoration algorithms using maximum a posteriori estimations with application to fluorescence microscopy.* Journal of the Optical Society of America a-Optics Image Science and Vision, 1997. **14**(8): p. 1696-1706.
3. Gibson, S.F. and F. Lanni, *DIFFRACTION BY A CIRCULAR APERTURE AS A MODEL FOR 3-DIMENSIONAL OPTICAL MICROSCOPY.* Journal of the Optical Society of America a-Optics Image Science and Vision, 1989. **6**(9): p. 1357-1367.
4. Vermolen, B.J., et al., *3D nuclear organization of telomeres in normal and cancerous mammalian cells.* Cytometry Part A, 2004. **59A**(1): p. 97-97.

5. Luengo Hendriks, C.L., et al., *DIPimage, a scientific image processing toolbox for MATLAB.* 1999, Pattern Recognition Group, Department of Applied Physics, Delft University of Technology.
6. Vermolen, B.J., et al., *Segmentation and Analysis of the Three-Dimensional Redistribution of Nuclear Components in Human Mesenchymal Stem Cells.* Cytometry Part A, 2008. **73A**: p. 816-824.
7. Danielsson, P.E., *EUCLIDEAN DISTANCE MAPPING.* Computer Graphics and Image Processing, 1980. **14**(3): p. 227-248.
8. Mullikin, J.C., *THE VECTOR DISTANCE TRANSFORM IN 2 AND 3 DIMENSIONS.* Cvgip-Graphical Models and Image Processing, 1992. **54**(6): p. 526-535.
9. Lansdorp, P., et al., *Heterogeneity in telomere length of human chromosomes.* Hum. Mol. Genet., 1996. **5**(5): p. 685-691.
10. Verwer, B.J.H., L.J.v. Vliet, and P.W. Verbeek, *Binary and grey-value skeletons: metrics and algorithms.* International Journal of Pattern Recognition and Artificial Intelligence, 1993. **7**(5): p. 1287-1308.